Thermalizing channel states for rapid qubit heating

Ziyang You,^{1,2} Wenhui Huang,^{3,4} Libo Zhang,^{3,4} Song Liu,^{4,5} Youpeng Zhong,^{4,5} Yibo Gao,⁶ and Hou Ian^{1,*}

¹Institute of Applied Physics and Materials Engineering, University of Macau, Macau, China

²School of Electronic, Electrical Engineering and Physics,

Fujian University of Technology, Fuzhou, Fujian, China

³Shenzhen Institute for Quantum Science and Engineering,

Southern University of Science and Technology, Shenzhen, China

⁴International Quantum Academy, Shenzhen 518048, China

⁵Shenzhen Branch, Hefei National Laboratory, Shenzhen 518048, China

⁶School of Physics and Optoelectronic Engineering, Beijing University of Technology, Beijing, China

Although known for negatively impacting the operation of superconducting qubits, thermal baths are shown to exert qubit control in a positive way, provided they are properly engineered. We demonstrate an experimental method to engineer the transduction of microwave driving into heat flow through a leaky resonator. Given the precise conversion, a qubit receiving the heat flow obtains a quasi-thermal equilibrium with arbitrary target temperature in hundreds of nanoseconds. We show that the dynamics of the quantum transducing process is described by thermalizing channel states, generated from the double dressings of the resonator by the semi-classical driving and the qubit-resonator coupling. Their spectrum, coupling, and driving strength determine the channel rate of energy flow, along with the relaxation rates of photon leakage into the bath. The analytical prediction is shown to match well with the experimental measurements on an Xmon qubit circuit.

Introduction – The negative impact that the environment imposes on the operation of superconducting qubits is well known. Over the years, uninterrapted efforts are spent on analyzing the sources of these impacts, including bias noise [1], dielectric loss [2], 1/f flux noise [3], and two-level defects [4– 6], not to mention the many more studies on eliminating them. On the other hand, the concept of bath or reservoir engineering is introduced to dissipatively drive quantum systems into desired steady states [7, 8], including computationally meaningful ones [9]. The concept has been applied to system specific studies on optical cavities [10], spin chains [11], trapped ions [12], and Rydberg atoms [13] and has been experimentally verified on superconducting qubits [14–16], as well as atomic ensembles [17] and trapped ions [18–20]. In particular, when properly engineered, baths play a positive role in generating entanglement [16, 21]. Moreover, properly engineered baths can facilitate thermalization for various systems [22, 23] from a thermodynamic perspective.

In fact, quantum heat engines [24, 25] and subsequently quantum thermal machines (QTM) [26–29] have long been introduced to pursue the microscopic origin of prevalent concepts in thermo-statistical mechanics. Not only are work and entropy necessarily reformulated [30], the empirical thermo-dynamic laws are also tested [31–33] or even contested [34] for quantum systems. However, the controllability of such practical quantum systems as superconducting qubits [35] requires faster endothermal and exothermal processes for heat transfer, demanding specific bath-engineering techniques for QTM. The lack of such techniques explains the rapid theoretical development of quantum thermal cycles [36, 37] including the refinements on Otto cycles [38–41] and Carnot cycles [42–44] in contrast to the scarcity of their experimental implementations [45].

Seeing this need for a precisely controllable non-equilibrium process for sourcing thermal energy into superconducting

qubits, we develop a technique to transduce microwave driving into heat flux. The energy conversion is realized by thermalization channel states that are dressed from a leaky resonator by both the driving and its qubit coupling. Receiving the heat influx, the target qubit is rapidly saturated to a steady state on the order of hundred nanoseconds. We analytically derive the rate of transduction by solving a master equation established on the channel state spectrum. Experimently, by continuously monitoring the qubit inversion, we observe the transition of Rabi oscillation to saturation convergence while the resonator acting as the QTM is gradually switching on by its driving strength. According to this driving power as well as the qubitresonator detuning, the effective temperature is obtainable over the range from the equilibrating bath temperature up to infinity. The analytical prediction matches well with our experimental observations on an Xmon circuit.

Dynamically speaking, the qubit experiences a transition from an initial stage of coherent pumping to a stage of heat infusing. The evolution is therefore a hybridization of stimulated radiation at the beginning and spontaneous radiation that entails. Since the spontaneous absorption is sourced from the hybridized driving rather than a higher-temperature bath, the qubit reaches a hotter thermal state much faster than it would be with an equilibrating bath. The terminal steady state is thus a quasi-equilibrium state for the qubit, which balances the influxing transduced energy and the outfluxing dissipation. In addition, we note that the recently discovered inverse version [46] of quantum Mpemba effect [47–50] also enables fast heating of qubits. The qubit states are driven to higher doublets with a temporally interlaced sequence of coherent driving and relaxation. In contrast, the thermal photons in the channel states here are derived from mixing with the bath continuum, thus limiting the effective temperature to infinity instead of negative temperatures. A combination of the channel-state thermalization and inverse Mpemba effect could potentially

enable more versatile heating control to qubits.

Thermalizing channels - Transducing an external driving into a thermalizing energy flow requires a QTM to mediate between the qubit and the bath, without which the qubit would simply decay and emit energy. The existence of mediation creates thermalization channels, which are essentially intermediate levels that accentuate multi-photon processes across broad spectrum between the qubit and the driving. As illustrated in Fig. 1(a), these intermediate channel states are formed by a cavity mode dressing the two-level qubit whilst being pumped by a driving field. The poor quality and thus broad linewidth of the cavity permits frequent exchanges with the environment and retainment of photons across a finite band of frequencies, which are sourced from the monochromatic drive. On the other hand, when the qubit is biased to near-resonance with the cavity to form photon exchanges with the cavity via their Jaynes-Cummings coupling. Since the cavity photons have a continuous spectrum, it is equivalent to a multi-mode oscillator that models heat baths and induces spontaneous radiation of the qubit.

In our experiment, the target Xmon qubit Q_T of level spacing ω_q is coupled to an $\omega_r/2\pi = 5.445$ GHz stripline resonator, whose equivalent circuit is illustrated in Fig. 1(b). The low-Q resonator has a full-width at half-maximum (FWHM) linewidth of $\gamma_r/2\pi 1.2$ MHz. An external microwave field of frequency ω_d is driving it at various strength Ω , from a few kHz and a few MHz, along the waveguide at d etuning Δ_q with low reflection. When detuned from the resonator but resonant with the qubit, the microwave field at driving frequency $\omega_d/2\pi = \omega_q/2\pi = 5.46$ GHz propagates through the resonator and drives the qubit directly, resulting in the observed Rabi oscillation with a decaying envelope with relaxation time $T_1 = 5.2\mu$ s, as shown in Fig. 2(a). When the leaky cavity is closely resonant with the qubit tuned to $\omega_q/2\pi = 5.448 \text{ GHz}$ and with a microwave driving frequency $\omega_d/2\pi = 5.45 \text{ GHz}$ and strength $\Omega/2\pi = 2.0$ MHz, a thermalized steady state emerges after a short duration of population oscillation, as shown in Fig. 2(b) (Cf. Sec. I and II of [51] for experimental details).

In fact, thermalization behavior already arises in the detuned case (a) in the form of prolonged Rabi periods. The gradual prolongation is apparent when we compare the measured data points with the theoretical expectation, the red curve produced by numerically solving the Liouville-master equation $\dot{\rho}=\mathcal{L}[\rho]$. The superoperator \mathcal{L} on ρ accounts for both the oscillation dynamics derived from the waveguide QED Hamiltonian $H=\omega_q\sigma_z+\Omega(\sigma_+e^{-i\omega_dt}+\sigma_-e^{i\omega_dt})$ for the detuned case, where the driving strength is set to $\Omega/2\pi=5.2$ MHz, and the relaxation dynamics induced by the bath-related Lindbladians

Comparing the close-resonant scenario with the detuned case, the disappearance of Rabi oscillation which is substituted by the appearance of a steady state is explained by the formation of thermalization channels. On one hand, the resonator-qubit resonance essentially forms dressed states between these two subsystems. On the other, though the leaky resonator is

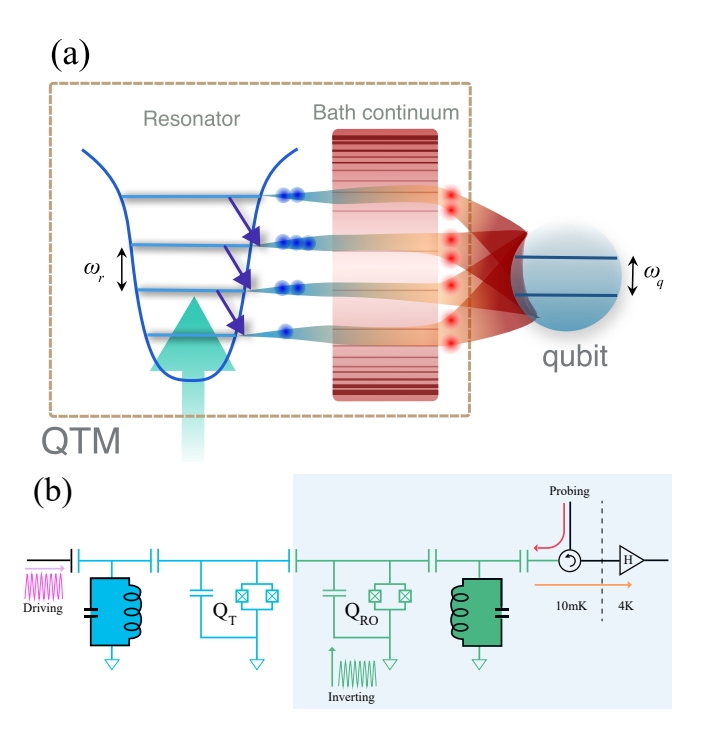


FIG. 1. (a) Conceptual illustration of thermalizing channels of the QTM constructed from hybridizing a resonator mode with a continuous multimode bath. While being energy fed by an external pump, the leaky resonator has its states broadened by bath couplings so that multi-photon resonance with the bath are engaged before photons are absorbed by the two-level qubit. The bath resonance essentially converts single-mode photons (blue circles) into broad-spectrum thermal photons (red circles) such that energy carried by the driving photons are rendered into a heat flow. The LC circuit represents the low-Q coplanar stripped waveguide that provides the resonator modes for generating the thermalizing channels. (b) Equivalent circuit on the superconducting qubit chip, where the target Xmon qubit Q_T while being driven from the left is monitored by a readout subcircuit (the shaded region) on the right. The readout is realized by a dispersively coupled qubit Q_{RO} , whose frequency shift is registered on another dedicated resonator.

constantly pumped by the resonant drive, the short-lived cavity photons are either exchanged into qubit excitations through the dressed states or spontaneously radiated into the surrounding bath. The latter results in thermal photons of differing frequencies spontaneously fedback from the broad spectral bath, which ultimately are injected into the qubit. In other words, instead of decayed as in equilibrating processes with the bath, the spontaneous emission and absorption are sustained, forming *channel states* that transfer thermal photon energy sourced from the driving and mediated by the bath into the qubit, as illustrated in Fig. 1(a).

Originating from the tripartite system, the channel states mix basis states from the 2n-dim Hilbert spaces of the qubit-resonator subsystem with the semi-classical driving terms. When they are equilibrating with a lower-temperature bath, the qubit state within the mixture approaches a steady state that is in quasi-equilibrium with the bath: the qubit inversion

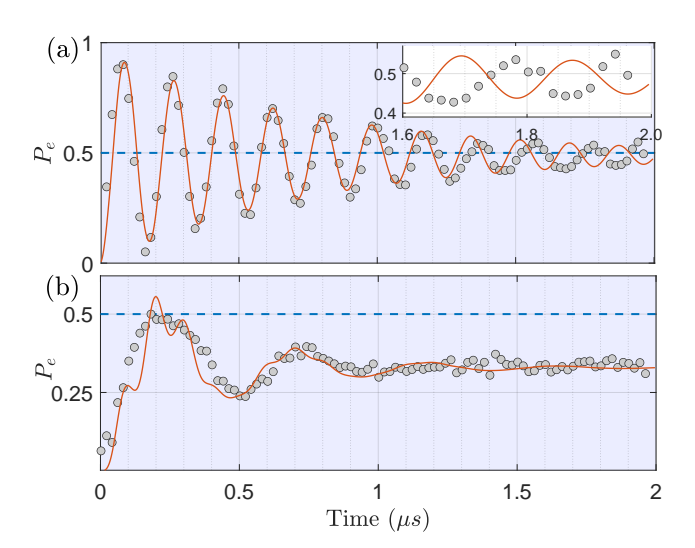


FIG. 2. Measured excited state population or inversion P_e (grey dots) of the Xmon qubit against time: (a) exhibiting Rabi oscillation (about the blue $P_e = 1/2$ dash line) when the driving frequency $\omega_d/2\pi = 5.46$ GHz is resonant with the qubit but far detuned from the leaky resonator frequency $\omega_r/2\pi = 5.445$ GHz; (b) exhibiting rapid convergence to a saturated level when $\omega_d/2\pi = 5.45$ GHz is simultaneously near resonant with both the qubit and the resonator, which is always under $P_e = 1/2$. The orange solid curve are theoretical fit computed from numerical methods. The inset shows that even when the resonator is far-detuned from the driving, the bath mediation is effective as the discrepancy becomes apparent between the measured P_e and the numerical prediction assuming only qubit-drive resonance, as time increases.

is saturated to an equivalent Gibbs temperature higher than the bath temperature, depending on the driving strength. In the case shown in Fig. 2(b), the qubit effective temperature T is 0.37 K while the bath temperature set by the dilution refrigerator is about 20 mK.

Non-equilibrium dynamics – To appreciate the experimental observations above from a theoretical perspective, we consider the quasi-equilibrium process generated by the interplay between the channel states and the bath be described by the master equation $\dot{\rho} = \mathcal{L}[\rho]$ under the driven Jaynes-Cumming (JC)-model Hamiltonian

$$H = \frac{\omega_q}{2}\sigma_z + \omega_r a^{\dagger} a + \eta (a^{\dagger}\sigma_- + a\sigma_+) + \Omega (a^{\dagger}e^{-i\omega_d t} + ae^{i\omega_d t}). \tag{1}$$

Shown as the solid curve in Fig. 2(b), the numerical solution [52] with a computational basis of 15 dimensions to the master equation fits well with the experimental measurements.

To sufficiently describe the energy converted from the coherent driving of strength Ω into an incoherent heat flow, we consider the channel states mentioned above as the eigenstates of Hamiltonian (1). Since the qubit-resonator coupling and the driving terms cannot be simultaneously diagonalized, approximations have to be sought. Methodology-wise, a typical circuit QED approach only diagonalize the η -coupling term while leaving the weak driving Ω as a perturbation. In the

opposite case where Ω is comparatively stronger than η , such as the interaction between a superconducting qubit and two-level oxide defects, the driving is diagonalized in the coherent state space while the η term is regarded as a pertubation [6]. Here, neither of these two cases applies since η and Ω are on similar orders of magnitude because the leaky resonator, while being coupled to the qubit, is rapidly driven to sustain the thermalization against the simultaneous relaxation. Without the perturbation approach, we use dimension truncation to make the theoretical analysis analytical, i.e. the number of channel states is limited to three, namely $\{|\mu_k\rangle: k=0,1,2\}$, which shall prove to be sufficient for interpreting the experimental results.

These three channel states diagonalize Hamiltonian (1) as $H_S = \sum_k \varepsilon_k |\mu_k\rangle \langle \mu_k|$ in the lowest energy dimensions [51] and are responsible for converting coherent energy from the drive into thermal energy. To substantiate this proposition, consider the master equation under the channel state basis

$$\dot{\rho} = -i \left[H_{S}, \rho \right] - \sum_{n,k \neq n} \Gamma_{kn} \left[\frac{1}{2} \left\{ |\mu_{n}\rangle\langle\mu_{n}|, \rho\right\} - |\mu_{n}\rangle\langle\mu_{k}| \rho |\mu_{k}\rangle\langle\mu_{n}| \right], \quad (2)$$

which is derived from perturbative analysis to a Liouville equation on the system and the bath [51]. The coefficients

$$\Gamma_{kn} = \left[\bar{\gamma}(\varepsilon_n - \varepsilon_k) + \bar{\gamma}(\varepsilon_k - \varepsilon_n) + \gamma(\varepsilon_k - \varepsilon_n)\right] \times \frac{\left(\eta(\Delta_k^{-1} + \Delta_n^{-1}) + \Omega(\varepsilon_k^{-1} + \varepsilon_n^{-1})\right)^2}{\left(1 + \eta^2 \Delta_k^{-2} + \Omega^2 \varepsilon_k^{-2}\right) \left(1 + \eta^2 \Delta_n^{-2} + \Omega^2 \varepsilon_n^{-2}\right)}$$
(3)

signifies the *channel rate*, in which $\bar{\gamma}(\omega)$ and $\gamma(\omega)$ indicate the contributions of spontaneous transitions induced by the bath at finite temperature and at vacuum, respectively, at a given frequency ω . Consequently, $\bar{\gamma}(\varepsilon_n - \varepsilon_k)$ for example indicates the rate of directional (from k-th to n-th channel state) spontaneous radiation associated with photon energy $\varepsilon_n - \varepsilon_k$ at the bath temperature (20mK of the dilution fridge). Moreover, as in the usual cases of master equations, the finite-temperature contribution is two-sided while the vacuum contribution is one-sided in their frequency distributions with respect to the bath spectrum. However, different from the usual cases, the Γ_{kn} here is modified by a factor (second line of the equation) determined by both η and Ω as well as the detunings Δ_k $\varepsilon_k - (\omega_q - \omega_d)$. At vanishing coupling strength η and weak driving Ω , Eq.(2) falls back to the usual master equation of a weakly driven qubit, whose trajectory would become those shown in Fig. 2(a). In addition, if Γ_{kn} vanishes by way of reducing $\bar{\gamma}$ and γ to vanishing values, the effect of driving would then embody only in the free evolution generated by $H_{\rm S}$, i.e. Rabi oscillations.

Thermal photon transduction – On the contrary, with finite coupling and sufficient driving, Γ_{kn} being the coefficient of the Lindbladian describes the channeling rate of energy towards the qubit. The factor of $\bar{\gamma}$ and γ , on one hand, demonstrates the

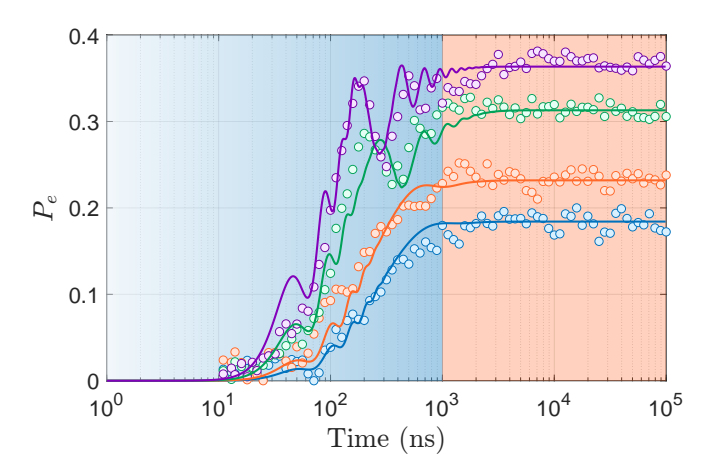


FIG. 3. Long-term population P_e variation of the qubit excited state on a semi-log scale over time at driving strengthes $\Omega/2\pi=1.5$ MHz (blue), 2 MHz (orange), 3.5 MHz (green), and 5 MHz (purple). The circled dots are the experimental measurements. The solid curves are theoretical predictions from the analytical solutions to the master equation using the same experimental Ω values as parameters, showing a great fit to the measurements. The background is shaded in two colors to visually discern the separation of two dynamic stages: (i) the light-blue endothermic stage and (ii) the light-orange quasi-equilibrium stage.

necessary presense of the bath to substantiate broadband photon exchanges; the factor of η and Ω , on the other, determines the conversion from coherent driving photons to spontanesouly radiated photons. When the driving photons following the circuit waveguide are incident on the resonator, some propagate through the resonator to directly invert the qubit, whereas the other leak into the bath and then are reabsorbed by the resonator before entering the qubit through resonator-qubit resonance. The time difference between these two processes causes a delay that separates the evolution dynamics into two stages from a thermodynamic perspective: (i) an endothermic stage and (ii) a quasi-equilibrium stage. As shown in Fig. 3 on a log-time scale, this two-stage distinction in dynamics is uniform across all driving strengthes where $\Omega/2\pi$ is 1.5, 2, 3.5, and 5 MHz for the four curves from bottom to top (See Sec. IV of [51] for the analytic derivations).

Starting from a bath-equilibrating ground state (due to the low environmental temperature), the qubit absorbs driving photons mediated by the resonator QTM. If the resonator has a high Q-factor as in typical circuit QED systems, qubit inversion would persist until the excited state population P_e approaches near unity; but the low-Q resonator permits rapid photon leakage into the bath, leaving room for photons to be refilled by the qubit. Hence, oscillations with local peaks much less than unity appear. Meanwhile, the leaked photons are fedback from the broad-spectrum bath as incoherent thermal photons and reabsorbed by the resonator. They would channel into the qubit via the channel states and give rise to an increasing mean that carries the coherent oscillation. These two processes, expressed by the two terms on the RHS of Eq. (2), compete with each other [6] and their concurrency effects the endorthermic

stage.

Later, when the population P_e accumulates, the upward and downward transition rates between the qubit states begin to reach a detailed balance and P_e would saturate at a steady value dependent on the driving strength Ω . Thermodynamically, it is the balance between the energy influx due to the driving and the energy outflux towards the bath, rather than a balance with the bath only. The stage appearing as a steady state is thus a quasi-equilibrium state: the qubit system remains out of equilibrium with the low-temperature bath throughout. For instance, while the bath remains at 20 mK, the four steady states in Fig. 3 correspond to effective temperatures 150 mK, 190 mK, 300 mK, and 450 mK, respectively, if we assume Gibbs distribution.

These experimental observations coincide with the theoretical results predicated by Eq. (2), which is exactly solvable. The non-diagonal elements ρ_{jk} ($j \neq k$) are decoupled and the first-order equation leads to a solution with negative real and imaginary exponentials of significant magnitudes. It signifies rapidly decaying transitions along with overriding oscillations among the channel states, which translates into a rapidly converging envelope on the order of μ s for the bare qubit state. Fast heating therefore appears during the endothermic stage, as we observe in Fig. 3. Simultaneously, the diagonal elements ρ_{kk} are coupled but still solvable by diagonalizing the transition matrix. The solution $\rho_{kk}(t)$, containing real exponentials $-\sum_{n,k\neq n} \Gamma_{kn}$, verifies the observation about rapid convergence above and predicts the steady state of the qubit inversion,

$$P_{e,SS} = \frac{1}{3} \sum_{k} \frac{\Omega^{2}}{\Omega^{2} + \varepsilon_{k}^{2} (1 + \eta^{2} / \Delta_{k}^{2})}$$
(4)

that is observed during the quasi-equilibrium stage. It becomes clear from Eq. (4) that the inversion at steady state in general increases with the driving strength Ω .

To be more specific, we have obtained the steady-state inversion at various driving frequencies and driving strengthes, which are plotted in Fig. 4. Effective temperatures are obtainable full range from near 0 to ∞ over the increase of Ω . In addition, enhancing qubit inversion is particularly conspicuous when the driving frequency is either $\omega_d/2\pi = 5.442$ or 5.457 GHz, which is neither resonant with the resonator nor the qubit. Rather, it conforms to the expectation of Eq. 3 that the channeling rates are maximized when the channel states frequencies ε_k and their detunings Δ_k from the relative qubit frequency δ_q are simultaneously optimized. Given the two factors in the equation, ε_k would need to match, on one hand, the bath spectrum to maximize the spontaneous resonator-bath photon exchange and atone, on the other hand, to η such that the exchanged photons are synchronously reabsorbed by the qubit.

In summary, we introduce a method of transduction to convert coherent driving into heat infusion on superconducting qubits. The experiment is conducted using a leaky and thus strongly bath-coupled resonator as an interface between the

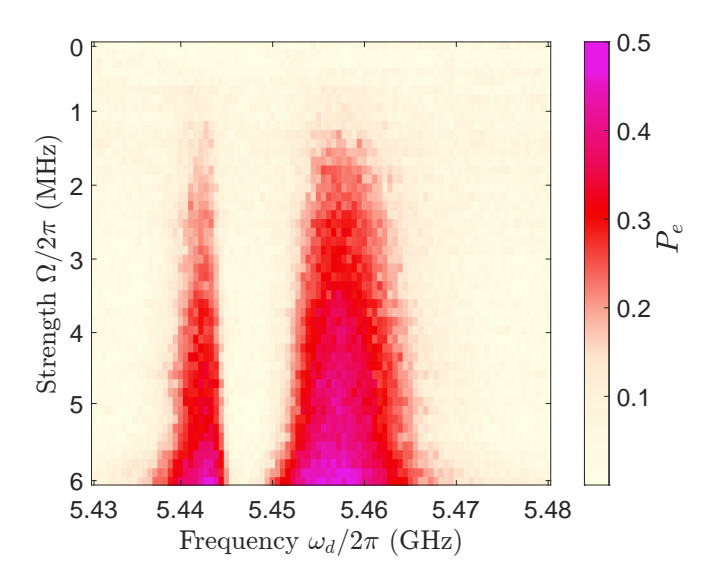


FIG. 4. Qubit inversion P_e plotted (a) as contour level against the driving frequency ω_d and driving strength Ω ; and (b) against ω_d only at the fixed strength $\Omega/2\pi = 5.8$ MHz.

driving and a target qubit. Depending on the driving parameters, full range of effective temperatures is observed at quasi-equilibrium after 100s of nanosecond. The rapid heating is theoretically explained by the existence of channel states identified as the diagonalizing states of the tripartite system comprising the qubit, the resonator, and the driving. They serve as the mediator with the bath to convert single-mode photons into thermal broadband photons, resulting in a channel transduction rate determined by the strength and detuning of the driving and the bath spectrum. The method permits simplified implementations of quantum thermal processes and cycle on superconducting qubits.

Y.-P. Z. thanks the support of NSFC of China under grant 12174178 and the Science, Technology and Innovation Commission of Shenzhen Municipality under grant KQTD20210811090049034. H. I. thanks the support of FDCT of Macau under grants 0179/2023/RIA3.

- * houian@um.edu.mo
- [1] J. M. Martinis, S. Nam, J. Aumentado, K. M. Lang, and C. Urbina, Decoherence of a superconducting qubit due to bias noise, Phys. Rev. B 67, 094510 (2003).
- [2] J. M. Martinis et al., Decoherence in Josephson Qubits from Dielectric Loss, Phys. Rev. Lett. 95, 210503 (2005).
- [3] F. Yoshihara, K. Harrabi, A. O. Niskanen, Y. Nakamura, and J. S. Tsai, Decoherence of Flux Qubits due to \$1/f\$ Flux Noise, Phys. Rev. Lett. 97, 167001 (2006).
- [4] R. McDermott, Materials Origins of Decoherence in Superconducting Qubits, IEEE Tran. Appl. Supercond. 19, 2 (2009).
- [5] S. Schlör, J. Lisenfeld, C. Müller, A. Bilmes, A. Schneider, D. P. Pappas, A. V. Ustinov, and M. Weides, Correlating Decoherence in Transmon Qubits: Low Frequency Noise by Single Fluctuators, Phys. Rev. Lett. 123, 190502 (2019).

- [6] Y. Wang, Z. You, and H. Ian, Dynamic Phases Induced by Two-Level System Defects on Driven Qubits, AVS Quan. Sci. 5, 036201 (2023).
- [7] J. F. Poyatos, J. I. Cirac, and P. Zoller, Quantum Reservoir Engineering with Laser Cooled Trapped Ions, Phys. Rev. Lett. 77, 4728 (1996).
- [8] P. M. Harrington, E. J. Mueller, and K. W. Murch, Engineered dissipation for quantum information science, Nat. Rev. Phys. 4, 660 (2022).
- [9] F. Verstraete, M. M. Wolf, and J. Ignacio Cirac, Quantum computation and quantum-state engineering driven by dissipation, Nat. Phys. 5, 633 (2009).
- [10] M. J. Kastoryano, F. Reiter, and A. S. Sørensen, Dissipative Preparation of Entanglement in Optical Cavities, Phys. Rev. Lett. 106, 090502 (2011).
- [11] G. Morigi, J. Eschner, C. Cormick, Y. Lin, D. Leibfried, and D. J. Wineland, Dissipative Quantum Control of a Spin Chain, Phys. Rev. Lett. 115, 200502 (2015).
- [12] D. C. Cole, J. J. Wu, S. D. Erickson, P.-Y. Hou, A. C. Wilson, D. Leibfried, and F. Reiter, Dissipative preparation of W states in trapped ion systems, New J. Phys. 23, 073001 (2021).
- [13] D. W. Schönleber, C. D. B. Bentley, and A. Eisfeld, Engineering thermal reservoirs for ultracold dipole–dipole-interacting Rydberg atoms, New J. Phys. 20, 013011 (2018).
- [14] M. E. Kimchi-Schwartz, L. Martin, E. Flurin, C. Aron, M. Kulkarni, H. E. Tureci, and I. Siddiqi, Stabilizing Entanglement via Symmetry-Selective Bath Engineering in Superconducting Qubits, Phys. Rev. Lett. 116, 240503 (2016).
- [15] Y. Lu, S. Chakram, N. Leung, N. Earnest, R. K. Naik, Z. Huang, P. Groszkowski, E. Kapit, J. Koch, and D. I. Schuster, Universal Stabilization of a Parametrically Coupled Qubit, Phys. Rev. Lett. 119, 150502 (2017).
- [16] T. Brown, E. Doucet, D. Ristè, G. Ribeill, K. Cicak, J. Aumentado, R. Simmonds, L. Govia, A. Kamal, and L. Ranzani, Trade off-free entanglement stabilization in a superconducting outrit-qubit system, Nat. Comm. 13, 3994 (2022).
- [17] H. Krauter, C. A. Muschik, K. Jensen, W. Wasilewski, J. M. Petersen, J. I. Cirac, and E. S. Polzik, Entanglement Generated by Dissipation and Steady State Entanglement of Two Macroscopic Objects, Phys. Rev. Lett. 107, 080503 (2011).
- [18] Y. Lin, J. P. Gaebler, F. Reiter, T. R. Tan, R. Bowler, A. S. Sørensen, D. Leibfried, and D. J. Wineland, Dissipative production of a maximally entangled steady state of two quantum bits, Nature 504, 415 (2013).
- [19] D. C. Cole, S. D. Erickson, G. Zarantonello, K. P. Horn, P.-Y. Hou, J. J. Wu, D. H. Slichter, F. Reiter, C. P. Koch, and D. Leibfried, Resource-Efficient Dissipative Entanglement of Two Trapped-Ion Qubits, Phys. Rev. Lett. 128, 080502 (2022).
- [20] M. W. van Mourik, E. Zapusek, P. Hrmo, L. Gerster, R. Blatt, T. Monz, P. Schindler, and F. Reiter, Experimental Realization of Nonunitary Multiqubit Operations, Phys. Rev. Lett. 132, 040602 (2024).
- [21] K. G. H. Vollbrecht, C. A. Muschik, and J. I. Cirac, Entanglement Distillation by Dissipation and Continuous Quantum Repeaters, Phys. Rev. Lett. 107, 120502 (2011).
- [22] Y. Yanay and A. A. Clerk, Reservoir engineering with localized dissipation: Dynamics and prethermalization, Phys. Rev. Res. 2, 023177 (2020).
- [23] J. P. Pekola and B. Karimi, Quantum thermalization via multiwave mixing, Phys. Rev. Res. 6, L042023 (2024).
- [24] T. D. Kieu, The Second Law, Maxwell's Demon, and Work Derivable from Quantum Heat Engines, Phys. Rev. Lett. 93, 140403 (2004).
- [25] H. T. Quan, P. Zhang, and C. P. Sun, Quantum Heat Engine with

- Multilevel Quantum Systems, Phys. Rev. E 72, 056110 (2005).
- [26] F. Tonner and G. Mahler, Autonomous quantum thermodynamic machines, Phys. Rev. E 72, 066118 (2005).
- [27] B. Leggio, B. Bellomo, and M. Antezza, Quantum Thermal Machines with Single Nonequilibrium Environments, Phys. Rev. A 91, 012117 (2015).
- [28] B. Bhandari, P. T. Alonso, F. Taddei, F. von Oppen, R. Fazio, and L. Arrachea, Geometric Properties of Adiabatic Quantum Thermal Machines, Phys. Rev. B 102, 155407 (2020).
- [29] L. M. Cangemi, C. Bhadra, and A. Levy, Quantum engines and refrigerators, Phys. Rep. 1087, 1 (2024).
- [30] L. Arrachea, Energy dynamics, heat production and heat—work conversion with qubits: toward the development of quantum machines, Rep. Prog. Phys. 86, 036501 (2023).
- [31] F. Brandão, M. Horodecki, N. Ng, J. Oppenheim, and S. Wehner, The Second Laws of Quantum Thermodynamics, Proc. Nat. Acad. Sci. 112, 3275 (2015).
- [32] B. de Lima-Bernardo, Unraveling the Role of Coherence in the First Law of Quantum Thermodynamics, Phys. Rev. E 102, 062152 (2020).
- [33] C. Xi, X. Liu, H. Liu, K. Huang, X. Long, D. Ebler, X. Nie, O. Dahlsten, and D. Lu, Experimental Validation of Enhanced Information Capacity by Quantum Switch in Accordance with Thermodynamic Laws, Phys. Rev. Lett. 133, 040401 (2024).
- [34] P. Lipka-Bartosik, M. Perarnau-Llobet, and N. Brunner, Operational Definition of the Temperature of a Quantum State, Phys. Rev. Lett. 130, 040401 (2023).
- [35] J. P. Pekola, Towards Quantum Thermodynamics in Electronic Circuits, Nat. Phys. 11, 2 (2015).
- [36] H. T. Quan, Y. Liu, C. P. Sun, and F. Nori, Quantum thermodynamic cycles and quantum heat engines, Phys. Rev. E 76, 031105 (2007).
- [37] H. Ian, Thermodynamic Cycle in a Cavity Optomechanical System, J. Phys. B: At. Mol. Opt. Phys. 47, 135502 (2014).
- [38] B. Karimi and J. P. Pekola, Otto Refrigerator Based on a Superconducting Qubit: Classical and Quantum Performance, Phys. Rev. B 94, 184503 (2016).
- [39] M. Kloc, P. Cejnar, and G. Schaller, Collective Performance of a Finite-Time Quantum Otto Cycle, Phys. Rev. E 100, 042126 (2019).
- [40] A. Solfanelli, M. Falsetti, and M. Campisi, Nonadiabatic Single-Qubit Quantum Otto Engine, Phys. Rev. B 101, 054513 (2020).
- [41] M. Łobejko, T. Biswas, P. Mazurek, and M. Horodecki, Catalytic Advantage in Otto-like Two-Stroke Quantum Engines, Phys. Rev. Lett. 132, 260403 (2024).
- [42] G. Xiao and J. Gong, Construction and Optimization of a Quantum Analog of the Carnot Cycle, Phys. Rev. E 92, 012118 (2015).
- [43] R. Dann and R. Kosloff, Quantum Signatures in the Quantum Carnot Cycle, New J. Phys. **22**, 013055 (2020).
- [44] P. Fadler, A. Friedenberger, and E. Lutz, Efficiency at Maximum Power of a Carnot Quantum Information Engine, Phys. Rev. Lett. 130, 240401 (2023).
- [45] J. P. S. Peterson, T. B. Batalhão, M. Herrera, A. M. Souza, R. S. Sarthour, I. S. Oliveira, and R. M. Serra, Experimental Characterization of a Spin Quantum Heat Engine, Phys. Rev. Lett. 123, 240601 (2019).
- [46] S. A. Shapira, Y. Shapira, J. Markov, G. Teza, N. Akerman, O. Raz, and R. Ozeri, Inverse Mpemba Effect Demonstrated on a Single Trapped Ion Qubit, Phys. Rev. Lett. 133, 010403 (2024).
- [47] A. K. Chatterjee, S. Takada, and H. Hayakawa, Quantum Mpemba Effect in a Quantum Dot with Reservoirs, Phys. Rev. Lett. 131, 080402 (2023).
- [48] L. Kh. Joshi et al., Observing the Quantum Mpemba Effect in Quantum Simulations, Phys. Rev. Lett. 133, 010402 (2024).

- [49] M. Moroder, O. Culhane, K. Zawadzki, and J. Goold, Thermodynamics of the Quantum Mpemba Effect, Phys. Rev. Lett. 133, 140404 (2024).
- [50] J. Zhang et al., Observation of quantum strong Mpemba effect, Nat. Comm. 16, 301 (2025).
- [51] See supplementary materials.
- [52] J. R. Johansson, P. D. Nation, and F. Nori, QuTiP: An open-source Python framework for the dynamics of open quantum systems, Comp. Phys. Comm. 183, 1760 (2012).

Supplementary Materials to Thermalizing channel states for rapid qubit heating

Ziyang You, ¹ Wenhui Huang, ^{2,3} Libo Zhang, ^{4,3} Song Liu, ^{2,3} Youpeng Zhong, ^{2,3} Yibo Gao, ⁵ and Hou Ian ^{1,*}

¹Institute of Applied Physics and Materials Engineering, University of Macau, Macau, China

²Shenzhen Institute for Quantum Science and Engineering,
Southern University of Science and Technology, Shenzhen, China

³International Quantum Academy, Shenzhen 518048, China

⁴Shenzhen Institute for Quantum Science and Engineerin g,
Southern University of Science and Technology, Shenzhen, China

⁵School of Physics and Optoelectronic Engineering,
Beijing University of Technology, Beijing, China

I. EXPERIMENTAL SETUP

The experimental setup is established on a general purposed superconducting circuit with two effective Xmon qubits [1] working in serial connection, as depicted in the circuit diagram in Fig. 1. Each qubit is coupled to a cavity. The target qubit, denoted as Q_T , is connected to a fast-decay cavity that constitutes the main part of the QTM model introduced in the main text. The second qubit Q_{RO} is responsible for detecting Q_T and is dispersively coupled to a readout cavity. This readout cavity is connected to a probing signal via a Purcell filter, which suppresses resonator-mediated qubit decay [2]. The probing response signal, reflected from the readout resonator, is routed through a circulator for

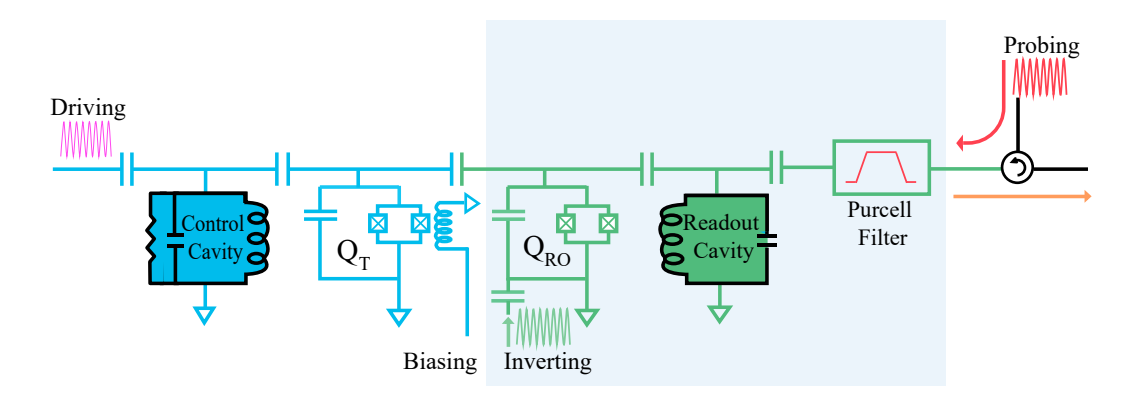


Figure 1. The circuit diagram of the testing chip. A specialized readout protocol is employed, where Q_{RO} serves as an ancillary prober to read out the state of the test qubit. The components in the entire shaded region function as an equivalent readout cavity coupled to the target qubit Q_T .

^{*} houian@um.edu.mo

System parameters	Target qubit Q_T	Ancillary qubit Q_{RO}
Qubit frequency	5.46 GHz	3.81 GHz
Frequency of coupling resonator	$5.445~\mathrm{GHz}$	$5.32~\mathrm{GHz}$
Qubit-resonator coupling strength	4 MHz	32 MHz
Qubit-qubit coupling strength	$100~\mathrm{MHz}$	
Qubit relaxation time	$5.2~\mu \mathrm{s}$	$26~\mu \mathrm{s}$
Resonator linewidth	1.2 MHz	1.3 MHz

Table I. Parameters measured on the target and the ancillary qubits, along with their coupling resonators. Under the setting for forming the thermalizing channels, target qubit Q_T is near resonant with a control resonator.

analysis. To perform state tomography on Q_T , we employ a specialized readout protocol, using all three components in the shaded region equivalently as a conventional readout resonator.

The circuit chip is fabricated on a c-plane sapphire substrate with an approximately 100 nm thick aluminum layer, deposited using a high-vacuum e-beam evaporator system. The circuit geometries, excluding the junctions, are patterned through photolithography and etched using an inductively coupled plasma (ICP) dry etcher with BCl3/Cl2. The Josephson junctions are patterned via e-beam lithography and fabricated through double-angle evaporation of aluminum followed by liftoff. The measured parameters of the qubits and the resonators are summarized in Tab. I.

II. READOUT METHODOLOGY

In systems where the qubit has a dedicated readout resonator, the control and readout pulse sequences include a probing pulse applied to the resonator after qubit manipulation. The response to this probing pulse detects the state-dependent frequency shift in the resonator, revealing the qubit state. However, in our circuit fashioned from a general purposed sample chip, target qubit Q_T lacks a dedicated readout resonator to directly measure this state-dependent shift. Instead, a modified readout technique is employed, where the state of Q_T is mapped onto a Q_{RO} via their inter-qubit dispersive coupling, rather than relying on a resonator [3].

As shown in Fig. 1, an additional inverting pulse is applied to the ancillary qubit Q_{RO} after the manipulation of Q_T . It is a π pulse that fully inverts Q_{RO} when Q_T stays in the ground state. The population of Q_{RO} is subsequently read out by its dedicated readout resonator with high fidelity. The final population of Q_{RO} changes under the same inverting pulse due to the difference in absorption, depending on the state of Q_T . As a result, Q_T state can be inferred with good contrast through the Q_{RO} population using this approach, eliminating the need for a dedicated readout resonator.

Details of the apparatus setup are shown in Fig. 2. The sample chip is placed in an aluminum box and mounted in a dilution refrigerator, which maintains a base temperature of approximately 20 mK during measurements. Control and readout pulses for the testing system are generated using IQ modulation. These pulses are shaped in IQ mixers by combining a local oscillator (LO) signal with an envelope generated by arbitrary waveform generators (AWG). A high-precision DC source is used for local flux control of the qubit through the Z-bias line.

After attenuation, the modulated signal is sent to the testing system. The readout response from the resonator is first amplified by a high electron mobility transistor (HEMT) amplifier at the 4 K stage, followed by a low-noise amplifier (LNA) at room temperature. The amplified signal is then

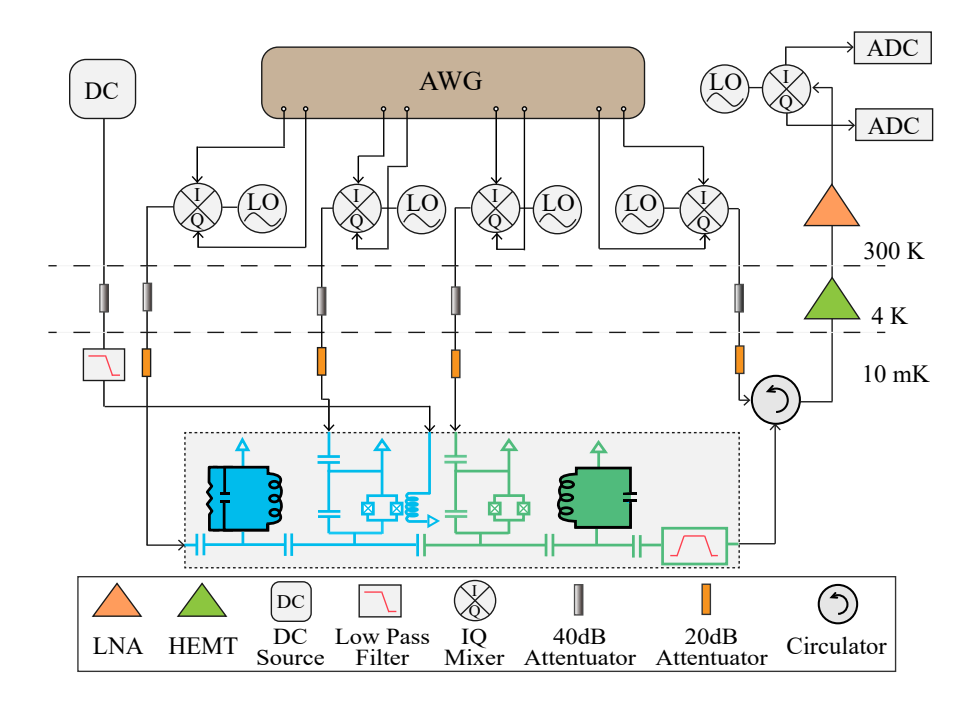


Figure 2. The signal chain of the experiment involves generating control and readout pulses using IQ modulation, combining a local oscillator (LO) signal with an envelope from an arbitrary waveform generator (AWG). The readout response is amplified by a high electron mobility transistor (HEMT) at 4 K and a low-noise amplifier (LNA) at room temperature, then demodulated in an IQ mixer and recorded by analog-to-digital converters (ADCs).

demodulated in an IQ mixer and recorded by analog-to-digital converters (ADCs).

III. CONSTRUCTING THE MASTER EQUATION

First, let the Hamiltonian in Eq. (1) of the main text be written as

$$H' = \frac{\omega_q}{2}\sigma_z + \omega_0 a^{\dagger} a + \eta (a\sigma_+ + a^{\dagger}\sigma_-) + \Omega(a^{\dagger} + a)$$
 (1)

in the rotating frame of the driving $V = \omega_d a^\dagger a + \omega_d \sigma_z$. If we truncate the Hilbert space dimension of the bare states to the lowest three, i.e. $\{|0,g\rangle,|1,g\rangle,|0,e\rangle\}$, and let the ground reference of the qubit be offset by $\omega_q/2$, the effective Hamiltonian is represented by the 3x3 matrix

$$H' \approx \begin{pmatrix} \delta_q & \eta & 0 \\ \eta & \delta_0 & \Omega \\ 0 & \Omega & 0 \end{pmatrix} \tag{2}$$

where the detunings are defined as $\delta_q = \omega_q - \omega_d$ and $\delta_0 = \omega_0 - \omega_d$. At close qubit-cavity resonance with $\delta_0 \approx \delta_q$, the eigenenergies of H' are the roots of the cubic equation

$$\varepsilon^3 - 2\delta_q \varepsilon^2 - (\Omega^2 + \eta^2 - \delta_q^2)\varepsilon + \Omega^2 \delta_q = 0.$$
 (3)

The associated depressed cubic is

$$\lambda^{3} - \left(\Omega^{2} + \eta^{2} + \frac{\delta_{q}^{2}}{3}\right)\lambda + \frac{\delta_{q}}{3}\left(\Omega^{2} - 2\eta^{2} + \frac{2\delta_{q}^{2}}{9}\right) = 0 \tag{4}$$

where $\lambda = \varepsilon - 2\delta_q/3$, giving the cubic root discriminant

$$\mathscr{D} = 4\eta^2 \delta_q^4 + (\Omega^4 + 20\Omega^2 \eta^2 - 8\eta^4) \delta_q^2 + 4(\Omega^2 + \eta^2)^3.$$
 (5)

Writing the δ_q^2 coefficient as $(\Omega^2 + (10 + 6\sqrt{3})\eta^2)(\Omega^2 + (10 - 6\sqrt{3})\eta^2)$, we recognize that as long as $\Omega > \sqrt{6\sqrt{3} - 10\eta}$ the discriminant is guaranteed positive, making Eq. 4 admit three real roots. Since the driving strength Ω and the coupling strength η is physically on the same order of magnitude, this inequality is easily satisfied; if not, \mathscr{D} would still have three real roots, where the inequality difference would be offset by the other positive terms. Therefore, we can solve the cubic equation by Viète's method, giving the roots

$$\varepsilon_k = \frac{2\delta_q}{3} + \frac{2\xi}{\sqrt{3}}\cos\frac{1}{3} \left[\cos^{-1}\frac{\sqrt{3}\delta_q(\delta_q^2/9 + 3\eta^2 - \xi^2)}{2\xi^3} + 2k\pi\right]$$
(6)

where k runs through $\{0,1,2\}$ and $\xi^2 = \Omega^2 + \eta^2 + \delta_q^2/3$. Since ε_k are distinct, they have unique eigenvectors

$$|\mu_k\rangle = \frac{\eta\varepsilon_k |0,e\rangle + \Delta_k\varepsilon_k |1,g\rangle + \Omega\Delta_k |0,g\rangle}{\sqrt{\eta^2\varepsilon_k^2 + \Delta_k^2\varepsilon_k^2 + \Omega^2\Delta_k^2}}$$
(7)

where $\Delta_k = \varepsilon_k - \delta_q$. In other words, Eq. (7) forming the new eigenbasis are the channel states that absorb driving energy and emit thermal energy, on which the system Hamiltonian is written as $H_{\rm S} = \sum_k \varepsilon_k |\mu_k\rangle \langle \mu_k|$. The annhilation operator is consequently expanded as

$$a = \sum_{j,k} \nu_{jk} |\mu_j\rangle \langle \mu_k| \tag{8}$$

and similarly for the creation operator, where

$$\nu_{jk} = \frac{\Omega \varepsilon_k}{\sqrt{\Omega^2 + \varepsilon_j^2 (1 + \eta^2 / \Delta_j^2)} \sqrt{\Omega^2 + \varepsilon_k^2 (1 + \eta^2 / \Delta_k^2)}}.$$
(9)

The master equation is obtained under the new basis by expanding the Liouville equation to the second perturbation order and tracing over the bath variables, i.e. for a universe density matrix $\rho(t) \otimes w$ at time t,

$$\frac{d\rho(t)}{dt} = -\int_{0}^{t} d\tau \operatorname{tr}_{B} \left\{ \left[\mathcal{H}(t), \left[\mathcal{H}(\tau), \rho(\tau) \otimes w \right] \right] \right\}$$
(10)

where $\mathcal{H}=\sum_j \kappa_j(a+a^\dagger)(b_j+b_j^\dagger)$ is the cavity-bath coupling Hamiltonian [4]. The coefficients κ_j determine the spectrum density of the bath and they contribute to the frequency dependent relaxation rate $\gamma(\omega)=2\pi\sum_j \kappa_j^2\delta(\omega-\omega_j)$ when assuming a typical Ohmic bath spectrum. During the system evolution, the bath being an energy reservoir remains stable and unentangled with the system such that the coupling $\mathcal{H}(t)=\sum_j \kappa_j(a(t)+a^\dagger(t))(b_j(t)+b_j^\dagger(t))$ at time t has the system and the bath operators remain orthogonal, i.e.

$$a(t) = e^{-iH_{S}t} a e^{iH_{S}t} = \sum_{j,k} \nu_{jk} e^{-i(\varepsilon_{j} - \varepsilon_{k})t} |\mu_{j}\rangle \langle \mu_{k}|$$
(11)

$$b_j(t) = b_j e^{-i\omega_j t} \tag{12}$$

With the customary Born-Markov approximation by assuming $\rho(t)$ a slow variable, the double commutator of Eq. (10) is traced to four integrable terms, with tracable factors reducing to

$$\operatorname{tr}_{B}\left\{\left(b_{j}^{\dagger}b_{j}e^{i\omega_{j}(t-\tau)}+b_{j}b_{j}^{\dagger}e^{-i\omega_{j}(t-\tau)}+\left(b_{j}^{2}e^{-i\omega_{j}(t+\tau)}+\operatorname{h.c.}\right)\right)w\right\}=\bar{n}_{j}e^{i\omega_{j}(t-\tau)}+(\bar{n}_{j}+1)e^{-i\omega_{j}(t-\tau)}$$
(13)

where inter-bath-mode correlations are ignored and \bar{n}_j denotes the average number of j-th mode thermal photons. To simplify the integration, we reverse the integration direction by letting $\tau \to (t-\tau)$ in Eq. (10) such that $(t-\tau) \to \tau$ and the integration range $\int_0^t d\tau$ remains unchanged. Then, expanding the commutators and taking the long-time limit $t \to \infty$, the first term reads

$$\sum_{j} \kappa_{j}^{2} \sum_{lkn} (\nu_{lk} + \nu_{kl}) (\nu_{kn} + \nu_{nk}) e^{-i(\varepsilon_{l} - \varepsilon_{k})t}$$

$$\int_{0}^{\infty} d\tau \left[\bar{n}_{j} e^{i\omega_{j}\tau} + (\bar{n}_{j} + 1) e^{-i\omega_{j}\tau} \right] e^{-i(\varepsilon_{k} - \varepsilon_{n})(t - \tau)} |\mu_{l}\rangle \langle \mu_{n}| \rho(t). \quad (14)$$

The exponentials are integrable via the usual analytic continuation of τ into the complex domain, where the integration path is closed via a semicircular loop with poles on the imaginary axis. The integral produces residues of delta functions such that Eq. (14) becomes

$$\sum_{lkn} (\nu_{lk} + \nu_{kl}) (\nu_{kn} + \nu_{nk}) e^{-i(\varepsilon_l - \varepsilon_n)t} \sum_j \pi \kappa_j^2 \left[\bar{n}_j \delta(\omega_j + \varepsilon_n - \varepsilon_k) + (\bar{n}_j + 1) \delta(\omega_j - \varepsilon_k + \varepsilon_n) \right] |\mu_l\rangle \langle \mu_n | \rho(t).$$
(15)

According to secular approximation [5, 6], the terms involving the discrete levels $\varepsilon_l \neq \varepsilon_n$ do not contribute to the bath couplings to the system modes. Thus, assigning respectively the finite- and the zero-temperature relaxation rates

$$\bar{\gamma}(\omega) = 2\pi \sum_{j} \kappa_{j}^{2} \bar{n}_{j} \delta(\omega_{j} - \omega), \tag{16}$$

$$\gamma(\omega) = 2\pi \sum_{j} \kappa_{j}^{2} \delta(\omega_{j} - \omega), \tag{17}$$

Eq. (14) eventually becomes

$$\sum_{k,n} \frac{\Gamma_{kn}}{2} |\mu_n\rangle \langle \mu_n| \rho(t). \tag{18}$$

The coefficients associated with the $|\mu_n\rangle$ term

$$\Gamma_{kn} = \frac{\Omega^2(\varepsilon_k + \varepsilon_n)^2}{(\Omega^2 + \varepsilon_k^2(1 + \eta^2/\Delta_k^2))(\Omega^2 + \varepsilon_n^2(1 + \eta^2/\Delta_n^2))} \left[\bar{\gamma}(|\varepsilon_k - \varepsilon_n|) + \gamma(\varepsilon_k - \varepsilon_n)\right],\tag{19}$$

combine the coupling strength η and the driving strength Ω with the relaxation rates $\bar{\gamma}$ and γ . They can be recognized as the energy channeling rates between the n-th and k-th channel states. In particular, given the definition of the relaxation rates, the zero and negative frequency rates vanish, i.e. $\gamma(\omega) = \bar{\gamma}(\omega) = 0$ whenever $\omega \leq 0$, for any quantum heat bath such as the ohmic bath. That means $\Gamma_{kk} = 0$ and either $\bar{\gamma}(\varepsilon_k - \varepsilon_n)$ or $\bar{\gamma}(\varepsilon_n - \varepsilon_k)$ survives for finite-temperature relaxation, thus the argument $|\varepsilon_k - \varepsilon_n|$ in Eq. (19). In other words, the contributions by finite-temperature relaxations are symmetric about the exchange of n and k, while that by zero-temperature relaxation are not.

The other three terms in the integral of Eq. (10) can be found using similar routines, giving rise to the master equation in Lindblad form

$$\dot{\rho} = -i \left[H_{S}, \rho \right] - \sum_{n} \left[\frac{\Gamma_{n}^{\circ}}{2} \left\{ \left| \mu_{n} \right\rangle \left\langle \mu_{n} \right|, \rho \right\} - \sum_{k \neq n} \Gamma_{kn} \left| \mu_{n} \right\rangle \left\langle \mu_{k} \right| \rho \left| \mu_{k} \right\rangle \left\langle \mu_{n} \right| \right]$$
(20)

where $\{\cdot,\cdot\}$ denotes the anti-commutator and $\Gamma_n^{\circ} = \sum_{k}' \Gamma_{nk}$ (the summation skips the k=n term) the total relaxation rate from the *n*-th channel state.

IV. SOLVING THE MASTER EQUATION

The master Eq. (20) can be solved by treating each element of the 3×3 density matrix $\rho(t)$ individually and solving its associated ordinary differential equation. That is, breaking up the master equation in its matrix elements, we have

$$\frac{d\rho_{jk}}{dt} = -i(\varepsilon_j - \varepsilon_k)\rho_{jk} - \left[\frac{\Gamma_j^{\circ} + \Gamma_k^{\circ}}{2}\rho_{jk} - \sum_{m \neq j} \Gamma_{mj}\delta_{jk}\rho_{mm}\right]. \tag{21}$$

Thus, for the non-diagonal elements $(j \neq k)$ and diagonal elements (j = k), we have respectively

$$\frac{d\rho_{jk}}{dt} = -\left[i(\varepsilon_j - \varepsilon_k) + \frac{\Gamma_j^{\circ} + \Gamma_k^{\circ}}{2}\right]\rho_{jk},\tag{22}$$

$$\frac{d\rho_{jj}}{dt} = -\Gamma_j^{\circ} \rho_{jj} + \sum_{m \neq j} \Gamma_{mj} \rho_{mm}. \tag{23}$$

Equation (22) can be directly inverted to find

$$\rho_{jk}(t) = \rho_{jk}(0) \exp\left\{-i(\varepsilon_j - \varepsilon_k) - \frac{\Gamma_j^{\circ} + \Gamma_k^{\circ}}{2}\right\} t$$
(24)

while Eq. (23) is also invertible by regarding it as the matrix differential equation $\dot{\boldsymbol{\rho}} = G\boldsymbol{\rho}$ where $\boldsymbol{\rho} = (\rho_{00}, \rho_{11}, \rho_{22})$ is the vector of the diagonal elements and

$$G = \begin{pmatrix} -\Gamma_0^{\circ} & \Gamma_{10} & \Gamma_{20} \\ \Gamma_{01} & -\Gamma_1^{\circ} & \Gamma_{21} \\ \Gamma_{02} & \Gamma_{12} & -\Gamma_2^{\circ} \end{pmatrix}. \tag{25}$$

The individual diagonal elements are solvable by diagonalizing G as $P^{-1}\Lambda P$. The corresponding eigenvalues, i.e. the diagonal elements of Λ , are the roots of

$$\lambda^3 + p\lambda^2 + q\lambda = 0 \tag{26}$$

where the coefficients are

$$p = \Gamma_0^{\circ} + \Gamma_1^{\circ} + \Gamma_2^{\circ}, \tag{27}$$

$$q = \Gamma_0^{\circ} \Gamma_1^{\circ} + \Gamma_1^{\circ} \Gamma_2^{\circ} + \Gamma_2^{\circ} \Gamma_0^{\circ} - \Gamma_{01} \Gamma_{10} - \Gamma_{12} \Gamma_{21} - \Gamma_{20} \Gamma_{02}.$$
(28)

Hence, besides $\lambda_0 = 0$, the non-zero roots are

$$\lambda_{\pm} = -\frac{1}{2} \sum_{j} \Gamma_{j}^{\circ} \pm \frac{1}{2} \sqrt{\sum_{j} \left[(\Gamma_{j}^{\circ} - \Gamma_{j+}^{\circ})^{2} + 4\Gamma_{jj} + \Gamma_{j+j} - \Gamma_{j+}^{\circ 2} \right]}$$
 (29)

where the index j is meant to iterate over $\{0, 1, 2\}$ and j^{\pm} denotes the modular increment or decrement, i.e. $(j \pm 1 \mod 3)$.

The analytical solution to Eq. (23) is then

$$\boldsymbol{\rho}(t) = P^{-1}e^{\Lambda t}P\boldsymbol{\rho}(0). \tag{30}$$

Considering that all the Γ are positive and the magnitude of $4\Gamma_{jj}+\Gamma_{j+j}$ is close to $\Gamma_{j}^{\circ 2}=(\Gamma_{jj}+\Gamma_{j-j})^2$, the discriminant of Eq. (29) is either positive (in most cases) or a small negative value (in rare cases). Even when the latter occurs, the dominant magnitude of λ_{\pm} is contributed by the real part of the Γ_j° sum. This shows the time evolutions of the diagonal elements given by Eq. (30) will mostly retain a decaying rather than oscillating form. On the other hand, given the relatively large magnitude of $(\varepsilon_j - \varepsilon_k)$, the non-diagonal elements given by Eq. (24) will be oscillating under the decaying envelopes.

V. QUASI-EQUILIBRIUM STATE

To obtain the steady state corresponding to the quasi-equilibrium limit, we can simply observe from Eq. (22) that the non-diagonal elements would approach zero as expected and from Eq. (23) that the steady state is just the non-trivial solution to the matrix equation associated with the G matrix in Eq. (25). The existence of the eigenvalue $\lambda_0 = 0$ shows that G is singular and the non-trivial solution is exactly the eigenvector corresponding to λ_0 , namely

$$\rho = \frac{1}{Z} \begin{bmatrix} \Gamma_1^{\circ} \Gamma_2^{\circ} - \Gamma_{12} \Gamma_{21} \\ \Gamma_2^{\circ} \Gamma_0^{\circ} - \Gamma_{20} \Gamma_{02} \\ \Gamma_0^{\circ} \Gamma_1^{\circ} - \Gamma_{10} \Gamma_{01} \end{bmatrix}$$
(31)

where Z denotes the normalization constant. Using the notation introduced in the last section, the vector elements can be summarized as

$$\rho_{kk} = \frac{\Gamma_{k^{+}}^{\circ} \Gamma_{k^{-}}^{\circ} - \Gamma_{k^{+}k^{-}} \Gamma_{k^{-}k^{+}}}{\sqrt{\sum_{j} \left[\Gamma_{j^{+}}^{\circ} \Gamma_{j^{-}}^{\circ} - \Gamma_{j^{+}j^{-}} \Gamma_{j^{-}j^{+}} \right]^{2}}}.$$
(32)

These diagonal elements are still in the channel state $\{|\mu_k\rangle\}$ basis. Using Eq. (7) and tracing out the cavity space, the excited state population can be found as

$$P_{e,SS} = \sum_{k} \rho_{kk}^{2} \left| \langle e, 0 | \mu_{k} \rangle \right|^{2}$$

$$= \sum_{k} \frac{\eta^{2} (\Gamma_{k}^{\circ} + \Gamma_{k}^{\circ} - \Gamma_{k+k} - \Gamma_{k-k}^{-})^{2}}{\eta^{2} + \Delta_{k}^{2} (1 + \Omega^{2} / \varepsilon_{k}^{2})} / \sum_{j} \left[\Gamma_{j}^{\circ} + \Gamma_{j}^{\circ} - \Gamma_{j+j} - \Gamma_{j-j}^{-} + \right]^{2}.$$
(33)

- [1] R. Barends et al., Coherent Josephson qubit suitable for scalable quantum integrated circuits, Phys. Rev. Lett. 111, 080502 (2013).
- [2] J. Heinsoo et al., Rapid high-fidelity multiplexed readout of superconducting qubits, Phys. Rev. Appl. 10, 034040 (2018).
- [3] C. Zhang, T.-L. Wang, L.-L. Guo, X.-Y. Yang, X.-X. Yang, P. Duan, Z.-L. Jia, W.-C. Kong, and G.-P. Guo, Characterization of tunable coupler without a dedicated readout resonator in superconducting circuits, Appl. Phys. Lett. 122 (2023).
- [4] C. Gardiner and P. Zoller, Quantum Noise: A Handbook of Markovian and Non-Markovian Quantum Stochastic Methods with Applications to Quantum Optics (Springer, 2004).
- [5] Cf. for instance, Sec.IV.B of C. Cohen-Tannoudji, J. Dupont-Roc, and G. Grynberg, Atom-Photon Interactions: Basic Processes and Applications (Wiley, 1998)
- [6] Cf. also Sec. 39 of L. D. Landau and E. M. Lifshitz, Quantum Mechanics (3rd edition, Pergammon, 1977).